Journal of Alloys and Compounds 693 (2017) 719–729

Contents lists available at ScienceDirect

Journal of Alloys and Compounds

journal homepage: http://www.elsevier.com/locate/jalcom

# Optical and X-ray induced luminescence from $Eu^{3+}$ doped $La_2Zr_2O_7$ nanoparticles

Madhab Pokhrel [a], Mataz Alcoutlabi [b], Yuanbing Mao [a, *]

[a] Department of Chemistry, University of Texas Rio Grande Valley, 1201 West University Drive, Edinburg, TX, 78539, USA
[b] Department of Mechanical Engineering, University of Texas Rio Grande Valley, 1201 West University Drive, Edinburg, TX, 78539, USA

ARTICLE INFO

*Article history:*
Received 22 June 2016
Received in revised form
3 September 2016
Accepted 20 September 2016
Available online 21 September 2016

*Keywords:*
Zirconates
Europium
Pyrochlore
Nanoparticles
Nanoscintillators

ABSTRACT

Nanocrystalline complex oxide scintillators have emerged for use in X-ray and gamma-ray detection in recent years. Here the doping concentration dependence of europium-doped lanthanum zirconate ($La_2Zr_2O_7$:xmol%$Eu^{3+}$, x = 1 to 35) nanoparticles (NPs) were investigated by using X-ray diffraction (XRD), X-ray photoelectron spectroscopy (XPS), Raman spectroscopy, scanning electron microscopy (SEM), and optically and X-ray excited luminescence. Spectroscopic methods revealed a gradual increase in disorder from the ordered pyrochlore structure to the defect fluorite structure as the $Eu^{3+}$ concentration increases. They showed red luminescence under charge transfer band (258 nm), and $Eu^{3+}$ 4f-4f bands (322, 394 and 465 nm) excitation with optical intensity dependent on the $Eu^{3+}$ doping concentration and not quenching up to 5% $Eu^{3+}$ doping concentration. The quantum yield of the red emission was found to depend on the $Eu^{3+}$ doping concentration and excitation wavelength. Moreover, these $La_2Zr_2O_7$:x%$Eu^{3+}$ NPs demonstrated an atypical $Eu^{3+}$ related scintillating response with a red emission under high-energy X-ray excitation with the scintillation intensity also depending on the $Eu^{3+}$ doping concentration. Finally, the irradiation damage behavior induced by the excitation source was representatively examined for the $La_2Zr_2O_7$:5%$Eu^{3+}$ NPs. It is expected that the current study will pave the way for future research of nanoscintillators.



## 1. Introduction

Rare earth (RE)-doped inorganic compounds have been widely used as phosphors and scintillators [1–6]. In addition, selected RE-doped inorganic compounds have also been used in fiber grating for realizing optical switching [7]. The properties of these RE elements and their multifaceted applications to science and industry are equally fascinating and have remained important as today [8]. Recently, there has been a great amount of interest in the derivative complex oxide structures, such as $A_2M_2O_7$ (A = $RE^{3+}$, and M = Ti, Sn, Zr, Hf) of dioxide $MO_2$type compounds as a RE host materials due to their binary metal cation sites [9–15]. The oxygen-deficient $A_2M_2O_7$-type compounds are achieved by the introduction of two oxygen vacancies during the charge-compensation for these dopants when $M^{4+}$ cations in $MO_2$ are replaced with trivalent cations of $A^{3+}$ [14,16]. These $A_2M_2O_7$ structures can exist in either the defect cubic fluorite ($Fm\bar{3}m$) or ordered pyrochlore ($Fd\bar{3}m$) crystal structure (Schematic 1). In general, the stability of the disordered fluorite structure is related to the ionic radius ratio of the A and M cations ($r_A/r_M$) and is favored for smaller lanthanides (<Gd) [11]. In the disordered fluorite structure, oxygen vacancies are randomly distributed on the anion site (8c) (Scheme 1a) and also known as defect or disordered fluorite structure. In ordered pyrochlore crystal structure, the A-site cations are 8-fold coordinated with oxygen and the M-site is 6-fold coordinated with oxygen (Scheme 1b).

Several synthesis routes have been used to prepare $A_2M_2O_7$ type powders, including the conventional solid-state mixing method (CSSM), hydrothermal synthesis, combustion synthesis, sol–gel synthesis and coprecipitation-calcination method [17–25]. Interestingly, synthesis of $A_2M_2O_7$ pyrochlore compositions by the combination of co-precipitation and molten salt synthesis (MSS) have been much less extensively studied when compared to other synthesis methods. Here, we confine our interests to trivalent $La^{3+}$ and tetravalent $Zr^{4+}$ to find phase stable pyrochlore $La_2Zr_2O_7$:x% $Eu^{3+}$ nanoparticles (NPs) below 1000 °C. There are two-steps for the co-precipitation-MSS method. First, a single-source complex

* Corresponding author.
*E-mail address:* yuanbing.mao@utrgv.edu (Y. Mao).

http://dx.doi.org/10.1016/j.jallcom.2016.09.218
0925-8388/

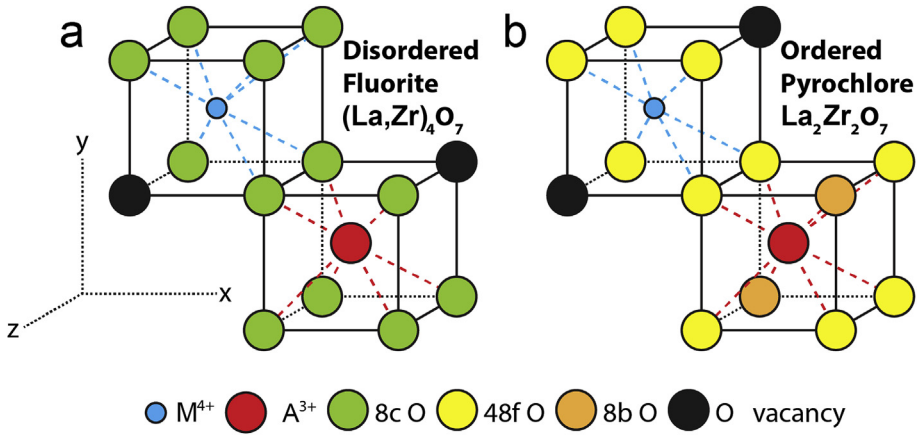


**Scheme 1.** Crystal structures of $La_2Zr_2O_7$: (a) defect fluorite structure where $La^{3+}$ and $Zr^{4+}$ occupy the unique cation site with 7-fold coordination; (b) ordered pyrochlore structure where $La^{3+}$ ion occupy the A-site with 8-fold co-ordination with oxygen. The smaller $Zr^{4+}$ cation occupies the M-site (16c) and is a 6-fold co-ordination with oxygen. Green, yellow, and orange spheres represent the oxygen on the 8c, 48f, and 8b sites, respectively.

precursor of $La(OH)_3{\cdot}x\%Eu(OH)_3{\cdot}ZrO(OH)_2{\cdot}nH_2O$ was synthesized via a co-precipitation route [26]. In the second step, $La_2Zr_2O_7$:x% $Eu^{3+}$ NPs were synthesized through a facile MSS process using the single-source precursors of hydroxides and nitrate salt mixture. In the MSS route, source precursors of hydroxides can be mixed thoroughly in the molten salt medium using a ball miller, facilitating the mixing and diffusion of reactant species and thus the subsequent reaction at a relatively low temperature. In addition, the synthesis generally can be carried out in regular crucibles without using an expensive setup.

$La_2Zr_2O_7$ is considered to be a highly dense material and proposed as a scintillator material in X-ray computed tomographic detectors [27–29]. Previous studies show that high density and high atomic number ($Z$) NPs can act as a sensitizer to enhance radiation dose delivered to tumors [30,31]. Thus, the combination of La and Zr in $La_2Zr_2O_7$ makes it a good host for X-ray attenuating properties and an excellent candidate for computed tomography contrast imaging agents in NP form. Recently, we have also shown that ordered pyrochlore based $La_2Zr_2O_7$:5mol%$Eu^{3+}$ NPs synthesized above 1000 °C possess lower photoluminescence (PL) quantum yield (QY) compared to that of disordered fluorite structure $La_2Zr_2O_7$:5mol%$Eu^{3+}$ NPs [32]. Interestingly, complex oxides such as $La_2Zr_2O_7$ have been investigated thoroughly to find the best radiation-tolerant materials that can be used as host materials for nuclear wastes or as advanced nuclear fuel in recent years [9,33–35]. Radiation tolerance refers to a material's ability to resist undesirable radiation-induced phenomena.

$Eu^{3+}$ is one of the most studied rare earth ions because of its unique Stokes emission characteristics [2,3,24,36–44]. In addition, it has a nearly monochromatic strong visible red emission around 612 nm. Importantly, there are already sufficient literature reports about the local structure of the $Eu^{3+}$ ion site that can be easily obtained from the f-f transition spectra [3,37,39,45–47]. The ground state ($^7F_0$) and excited state ($^5D_0$) of the $Eu^{3+}$ ion are non-degenerate and give information about the local symmetry and inhomogeneity of the surrounding ligands [38]. Therefore, $Eu^{3+}$ dopants can be used as probes to estimate the local structure of the host's ions.

In order to enhance the excitation and emission efficiency in $Eu^{3+}$ doped $La_2Zr_2O_7$ phosphors and develop its application as a phosphor and scintillator, it is necessary to find the optimized $Eu^{3+}$ concentration and understand the position of the broad charge transfer (CT) band position for excitation. It is also important to understand the correlation between the CT band of $Eu^{3+}$ doped $La_2Zr_2O_7$ and the crystal structure at different doping levels. To the best of our knowledge, no comparison report on the effect of dopant concentration on the PL and scintillation of defect fluorite structured $La_2Zr_2O_7$:x%$Eu^{3+}$ NPs has been reported under optical and X-ray excitation, respectively. Although observation of constituent elements has been carried out with X-ray photoelectron spectroscopy (XPS) for $La_2Zr_2O_7$ in previous studies [48,49], dopant concentration dependent XPS analysis has not been carried out before.

In this work, we studied $La_2Zr_2O_7$:x%$Eu^{3+}$ NPs (mole percentage x = 0, 1, 3, 5, 10, 15, 25, 30, and 35) under optical and X-ray excitation. Additionally, structural and morphological characteristics of the $La_2Zr_2O_7$:x%$Eu^{3+}$ NPs were investigated by X-ray diffraction (XRD), XPS, Raman spectroscopy, and scanning electron microscopy (SEM). We then studied their downconversion (Stokes) emission properties in the range of 500–750 nm with ultraviolet (258, 324, and 394), visible (465 nm) and X-ray excitations. In the analysis of the Stokes emission properties and mechanisms, we have included the dependence of the red emission intensity and the energy transfer process on the excitement wavelength. The $La_2Zr_2O_7$:x% $Eu^{3+}$ NPs also exhibit $Eu^{3+}$ related emissions under high energy X-ray excitation. We performed detailed studies on the effect of $Eu^{3+}$ doping concentration on the $La_2Zr_2O_7$ NP host, their PL, QY, and decay mechanisms including crystal structure. Finally, we examined the photo-stability of $La_2Zr_2O_7$:5%$Eu^{3+}$ NPs under different radiation exposures related by excitation sources.

## 2. Experimental section

### 2.1. Chemicals

The starting materials including lanthanum nitrate hexahydrate ($La(NO_3)_3{\cdot}6H_2O$, 99.0%), zirconium dinitrate oxide hydrate ($ZrO(NO_3)_2{\cdot}xH_2O$, 99.9%), europium(III) nitrate hexahydrate ($Eu(NO_3)_3{\cdot}6H_2O$, 99.9%), potassium nitrate ($KNO_3$, 99.9%), sodium nitrate ($NaNO_3$, 98%) and ammonium hydroxide ($NH_4OH$, 28.0–30.0%) were purchased from Sigma Aldrich. All chemicals are of analytical grade reagents and used directly without further purification.

### 2.2. Synthesis of $La_2Zr_2O_7$:x%$Eu^{3+}$ NPs

The $La_2Zr_2O_7$:x%$Eu^{3+}$ NPs (x = 0, 1, 3, 5, 10, 15, 25, 30, and 35) were prepared by a two-step co-precipitation-MSS process

following our previous reports [26,50,51]. First, a single-source complex precursor of $La(OH)_3{\cdot}x\%Eu(OH)_3{\cdot}ZrO(OH)_2{\cdot}nH_2O$ was synthesized via a co-precipitation route. In the second step, size-controlled $La_2Zr_2O_7$:x%$Eu^{3+}$ NPs were synthesized through a facile MSS process using the single-source complex precursors of $La(OH)_3{\cdot}x\%Eu(OH)_3{\cdot}ZrO(OH)_2{\cdot}nH_2O$ and nitrate mixture ($NaNO_3$:$KNO_3$ = 1:1, molar ratio) at 650 °C for 6 h. Further details can be found in ESI-1.

### 2.3. Characterization

Powder $La_2Zr_2O_7$:x%$Eu^{3+}$ NPs samples were characterized using X-ray diffraction (XRD), X-ray photoelectron spectroscopy (XPS), Raman spectroscopy, scanning electron microscopy (SEM), and optically and X-ray excited luminescence. Further details about instruments used, characterizations setup and measurement techniques can be found in ESI-2.

The excitation, kinetic scan, emission spectra and QY of the as-prepared $La_2Zr_2O_7$:x%$Eu^{3+}$ NPs were measured using an Edinburgh Instruments FLS980 fluorometer system. The details can also be found in our previous publications [32].

## 3. Results and discussion

### 3.1. Summary of the structural (XRD, SEM, EDX, and XPS) characterization

Powder XRD, Raman, SEM, EDX and XPS were used to characterize the crystalline phase, chemical composition, size and morphology of the $La_2Zr_2O_7$:xmol%Eu NPs. The XRD patterns of the examined $La_2Zr_2O_7$:x%Eu NPs are shown in Fig. 1 and correspond to defect cubic fluorite structure with space group $Fm\bar{3}m$ (PDF Card No. (JCPDS 73-0444). There are four prominent diffraction peaks. We refer to these reflections as parent fluorite peaks and index them as (222), (622), (440), and (400) assuming a structure with a fluorite unit cell. These peaks are the only allowed reflections in the angular range between (20–60°) for an oxide with the fluorite crystal structure, especially for those oxides close to the parent fluorite ($MO_2$) structures [10]. In addition, the intense and sharp diffraction peaks suggested well-crystallized samples. Within the detection limit of the X-ray diffractometer, no additional peaks were observed for any of our $La_2Zr_2O_7$:xmol%Eu NP samples. Specifically, the absence of typical super-lattice peaks at $2\theta = 27°$, 36°, 50°, etc. indicated that none of our products were found to have ordered pyrochlore type lattice based on XRD data [17]. The expanded view of the peak corresponding to (222) plane was shown in Fig. 1b, which clearly showed the broadening of the XRD peak with the increase of $Eu^{3+}$ dopant concentration. The peak shift towards higher angle clearly indicated that its lattice-spacing is decreasing (ESI-2) with increasing $Eu^{3+}$ doping concentration in $La_2Zr_2O_7$. This could be due to the lattice contraction caused by the difference in the ionic radii of $La^{3+}$ (130 pm) and $Eu^{3+}$ (118 pm). The doping of $Eu^{3+}$ into $La^{3+}$ site was further confirmed by EDX analysis (ESI-3).

SEM characterization was performed (Fig. S4) to assess the size and morphology of the $La_2Zr_2O_7$:xmol%$Eu^{3+}$ NPs. Morphologies of the as-prepared NPs were found to be regular and spherical. The average crystallite size of these NPs calculated using the Scherrer equation from XRD data ranged from 28 to 13 nm (ESI-5) with an average size of 20 ± 2 nm. Size calculations from SEM images confirmed these values of particle size from XRD calculations were accurate approximations (ESI-5).

### 3.2. Raman analysis

The absence of pyrochlore phase based on the XRD analysis could be due to the inability of XRD to resolve those diffraction peaks corresponding to pyrochlore phase. This is difficult since fluorite and pyrochlore structures have the same parent pattern and the emergence of minor reflections is the only indication of the pyrochlore structure, making accurate quantification by XRD analysis challenging.

Raman spectroscopy has been widely utilized as a tool to distinguish between defect-fluorite and ordered pyrochlore structured materials [22]. So we further investigated the compositions and structure of these NPs using Raman spectroscopy (Fig. 2).

Based on the group theory, the disordered fluorite $La_2Zr_2O_7$ with space group $Fm\bar{3}m$ has only one Raman active mode $T_{2g}$, where ordered pyrochlore with symmetry $Fd\bar{3}m$ possesses six peaks within the range of 200–1000 $cm^{-1}$ [52,53]. A detailed Raman spectroscopic characterization has been carried out on the $La_2Zr_2O_7$:x%Eu NPs in the range of 170–1000 $cm^{-1}$ (Fig. 2a and inset of Fig. 2b). In order to avoid the Eu luminescence interference with the Raman features of the $La_2Zr_2O_7$ host, an excitation wavelength of 785 nm was used. The spectrum from the $La_2Zr_2O_7$ host (Fig. 2b) consists of two strong bands at approximately 302 $cm^{-1}$ (1) and 504 $cm^{-1}$ (3) as well as four weak bands at about 386 $cm^{-1}$ (2), 633 $cm^{-1}$ (4), 733 $cm^{-1}$ (5) and 842 $cm^{-1}$ (6). The strongest band located at ~302 $cm^{-1}$ can be assigned to the $E_g$ internal La-O stretching mode and the bands at 386 $cm^{-1}$ and 504 $cm^{-1}$ are

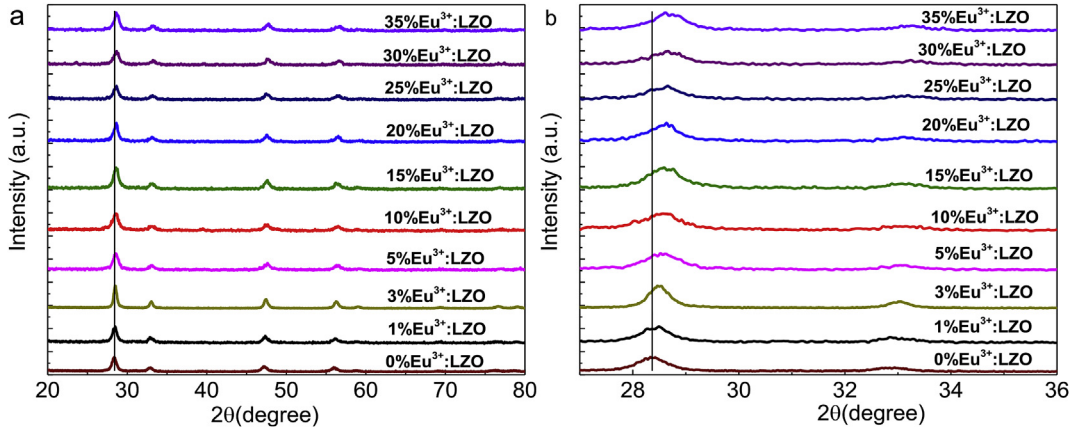


**Fig. 1.** (a) XRD patterns of the $La_2Zr_2O_7$:xmol%$Eu^{3+}$ NPs with x = 0, 1, 3, 5, 10, 15, 20, 25, 30 and (b) the enlarged view of the diffraction peak corresponding to the (222) plane at ~28.80°.

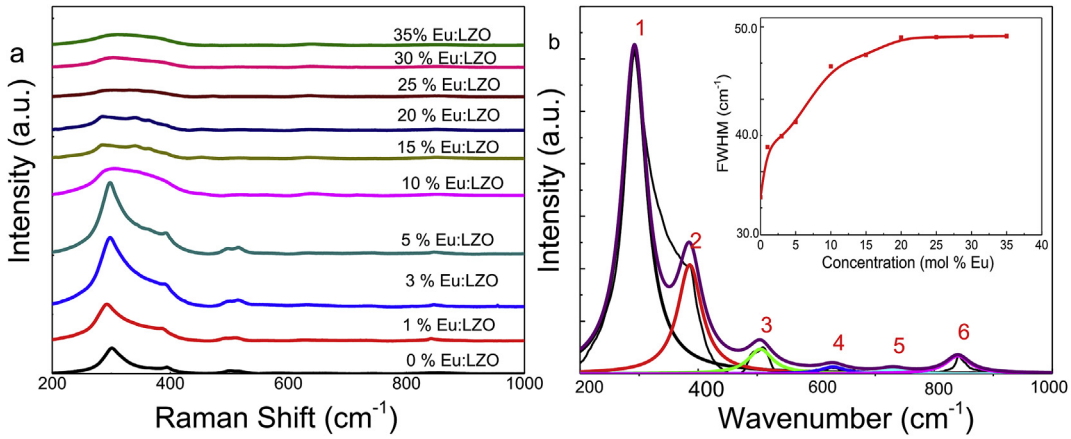


**Fig. 2.** (a) Raman spectra of the $La_2Zr_2O_7$:xmol%$Eu^{3+}$ NPs with x = 0, 1, 3, 5, 10, 15, 20, 25, 30 and 35. (b) Fitted Raman spectrum of the undoped $La_2Zr_2O_7$ NPs. Inset shows the FWHM at 302 $cm^{-1}$ of the $La_2Zr_2O_7$:xmol%$Eu^{3+}$ NPs with x = 0, 1, 3, 5, 10, 15, 20, 25, 30 and 35.

attributed to $T_{2g}$ modes of pyrochlore, respectively [52,54]. Peaks above 600 $cm^{-1}$ (633 $cm^{-1}$, 733 $cm^{-1}$ and the other band at 842 $cm^{-1}$) could be due to the distortion of the La site, which is coordinated in octahedral structure [55]. Peak shifts towards lower wavenumbers have been noticed after doping, especially at or above $La_2Zr_2O_7$:1%Eu compositions. The appearance of more than one internal stretching mode in the present samples ensures that these $La_2Zr_2O_7$:x%Eu NPs are not crystalized in the disordered fluorite structure as demonstrated from the XRD analysis. Comparing with other pyrochlore zirconates and hafnates, it could be seen clearly that Raman bands are sharp and ordered [55,56]. These Raman results clearly indicated that the $La_2Zr_2O_7$:x%Eu NPs synthesized using the coprecipitation-MSS method do not attain a pure defect fluorite structure contrary to results reported for low temperature synthesis by Kiel Holliday and et al. [57], but instead have a tendency to form a ordered pyrochlore structure. It has been well established that if the cations radius ratio {$La^{3+}$ (130 pm)/$Zr^{4+}$ (86 pm) = 1.51} is larger than 1.46, $A_2M_2O_7$ oxide becomes pyrochlore structure [17]. Therefore, it is not surprising that the zirconates with large $La^{3+}$ ions prepared in the present investigation appear to adopt an ordered pyrochlore lattice based on Raman data. As the radius ratio is decreased, one gets clear defect fluorite structure. In general, $Eu^{3+}$ doping ions are assumed to replace the $La^{3+}$ sites because of the same valence and small difference in $La^{3+}$ (130 pm) and $Eu^{3+}$ (118 pm) ionic radii. The broadening (Fig. 2b) and shift of this band (302 $cm^{-1}$) is evident for the doped samples, indicating the doping of Eu ion into the La sites. However, broadening is insignificantly small at lower $Eu^{3+}$ doping (inset of Fig. 2b), indicating that $Eu^{3+}$ ions are distributed uniformly replacing the $La^{3+}$ cation sites as expected. However, significant broadening (inset of Fig. 2b) and a decrease in the number of Raman peaks (Fig. 2a) indicated that there was an increase in localized disorder across the entire $La_2Zr_2O_7$ structure with higher $Eu^{3+}$ doping. Furthermore, we noticed that the ordered pyrochlore structure is gradually pushed towards disordered fluorite structure with higher $Eu^{3+}$ doping. This kind of structural change with $Eu^{3+}$ doping was unprecedented. However, this structural change with higher $Eu^{3+}$ doping becomes possible since the radius ratio of $Eu^{3+}/Zr^{4+}$ (1.37) is smaller than that of $La^{3+}/Zr^{4+}$ (1.51). Our observations showed some deviations from this range of stability of defect fluorite (<1.46), however, we believe that this theoretically evaluated limiting radius ratio should be used only as a broad guideline, or possibly only for undoped samples or bulk samples [17]. In summary, Raman analysis indicated that our $La_2Zr_2O_7$:x%$Eu^{3+}$ NPs possessed a pyrochlore structure. With the exception of un-doped and up to 5mol%$Eu^{3+}$ doped $La_2Zr_2O_7$ NPs, which showed all six Raman peaks, there was an evidence of anion disorder at higher $Eu^{3+}$ doping. The disorder of the anions, especially in the pyrochlore structure, resulted in the presence of broad Raman bands. It is worth to mention here that there is no extra crystal phase observed at doping up to 35% based on the XRD study. These observations are also consistent with the particle size, XPS analysis, excitation; emission and PL yield measurements discussed in later sections.

### 3.3. XPS analysis

It is well known that oxygen ions and oxygen vacancies are ordered across all anion sublattice sites in pyrochlore $La_2Zr_2O_7$ and one could anticipate that oxygen ions and vacancies are rearranged or destroyed with the addition of $Eu^{3+}$ ions [33]. Here, the possibility of $Eu^{3+}$ ion replacing the $Zr^{4+}$ regular sites cannot be completely discarded although they have very different ionic radii ($r_{Eu3+}$ = 118 pm and $r_{Zr4+}$ = 86 pm) and oxidation states. However, the substitution of $Eu^{3+}$ into the O sites is not feasible. Therefore, the changes in O 1s XPS spectra (Fig. 3) of the $La_2Zr_2O_7$:x%$Eu^{3+}$ NPs as a function of the Eu/La ratio could be a dopant ion effect. The photoelectron peaks of these samples are highly sensitive to dopant concentration. The O 1s profile is, in general, more complicated due to the overlapping contribution of oxygen from La and Zr in the case of $La_2Zr_2O_7$. The broad O 1s profile for low $Eu^{3+}$ doped sample could be due to random distribution of oxygen ions over many crystallographic equivalent sites [56]. This also points towards the existence of a high volume of oxygen defect states and disorders in undoped and 1% Eu doped $La_2Zr_2O_7$ NPs compared to those of the highly doped $La_2Zr_2O_7$:x%$Eu^{3+}$ NPs. This observation is consistent with the PL and QY analysis discussed below. However, two distinct oxygen peaks were observed for higher Eu doped samples indicating an ordered $La_2Zr_2O_7$ structure with oxygen ion redistribution. The spectral fitting demonstrated the O 1s binding energy (BE) peaks at approximately 529.6 eV and 532.0 eV. In the $La_2Zr_2O_7$ pyrochlore crystal structure, there are two oxygen sites at 48f and 8b (Scheme 1b). Six out of every seven oxygen ions occupy the 48f sites and each is coordinated by two lanthanum and two zirconium ions, and the seventh oxygen ion occupies the 8b site and is surrounded by four zirconium ions (Scheme 1b). This means that the electron density on oxygen for the La–O bond is higher than that of the Zr–O bond and could be the most possible reason for having two distinct binding energy peaks for O 1s in the $La_2Zr_2O_7$ crystal structure. So, this can be proposed as the combined effect of two

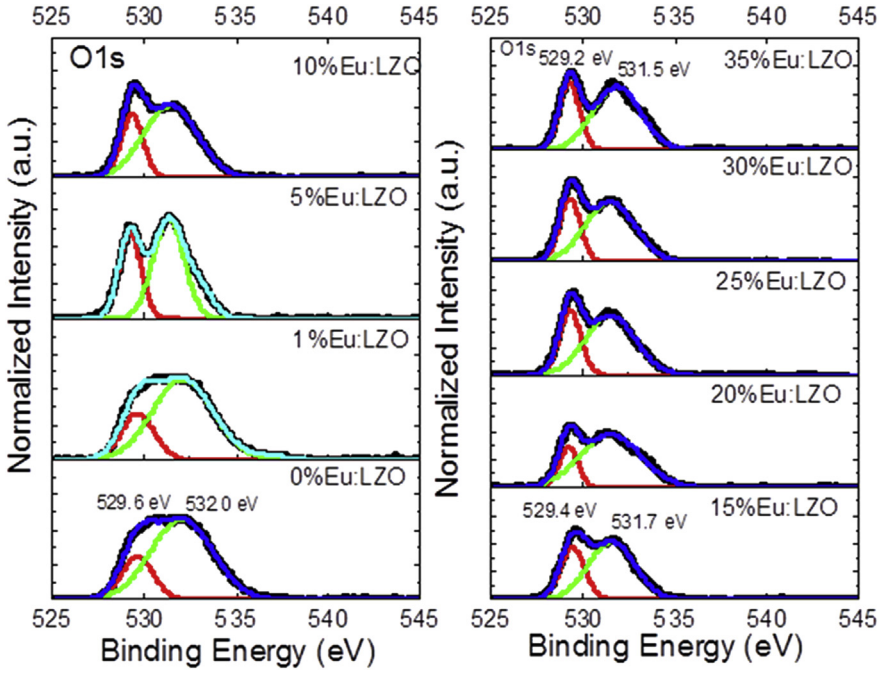


**Fig. 3.** O 1s XPS spectra of the as-prepared $La_2Zr_2O_7$:xmol%$Eu^{3+}$ NPs with x = 0, 1, 3, 5, 10, 15, 20, 25, 30 and 35.

metals with different ionicities in one binary oxide (i.e. La and Zr in the case of $La_2Zr_2O_7$) generating small BE shifts due to a specific redistribution of electron density during atomic ordering and crystal lattice formation [56,58]. Furthermore, the O 1s peak for the $La_2Zr_2O_7$:x%$Eu^{3+}$ NPs with higher $Eu^{3+}$ concentration shift to lower BE which can be simply related to the change in the broadening of the peak. The shift to lower BE was also observed for La 3d and Zr 3d (Figs. 4 and 5). In conclusion, the presence of two oxygen peaks on O 1s XPS spectra further supports the fact that these as-synthesized $La_2Zr_2O_7$:x%$Eu^{3+}$ NPs crystallizes in pyrochlore phase, which is consistent with the Raman analysis.

Fig. 4 shows the binding energies of the La 3d photoelectron peaks at 834.4, 838.3 and 851.1 eV for La $3d_{5/2}$ and La $3d_{3/2}$ lines, respectively. Small changes in BE indicate that the chemical state of lanthanum has changed slightly. However, the majority remained almost the same irrespective of dopant concentration. In addition, the absence of extra peaks and the shoulder peak ensures the purity of the compositions.

Fig. 5 shows the XPS spectra of Zr 3d from the as-prepared $La_2Zr_2O_7$:xmol%$Eu^{3+}$ NPs. The $Zr^{4+}$ 3d Gaussian-fitted profile

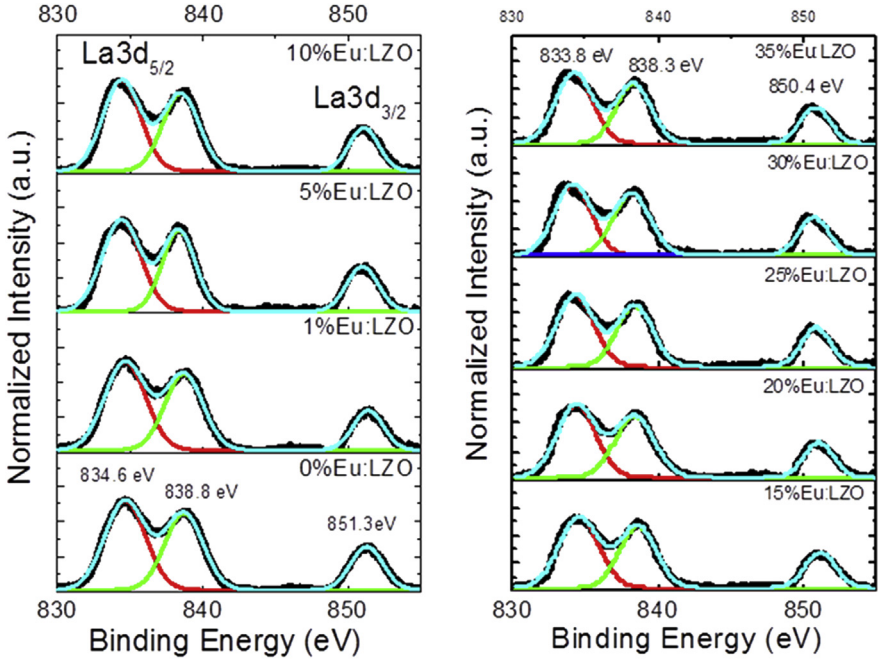


**Fig. 4.** La 3d XPS spectra of the as-prepared $La_2Zr_2O_7$:xmol%$Eu^{3+}$ NPs with x = 0, 1, 3, 5, 10, 15, 20, 25, 30 and 35.

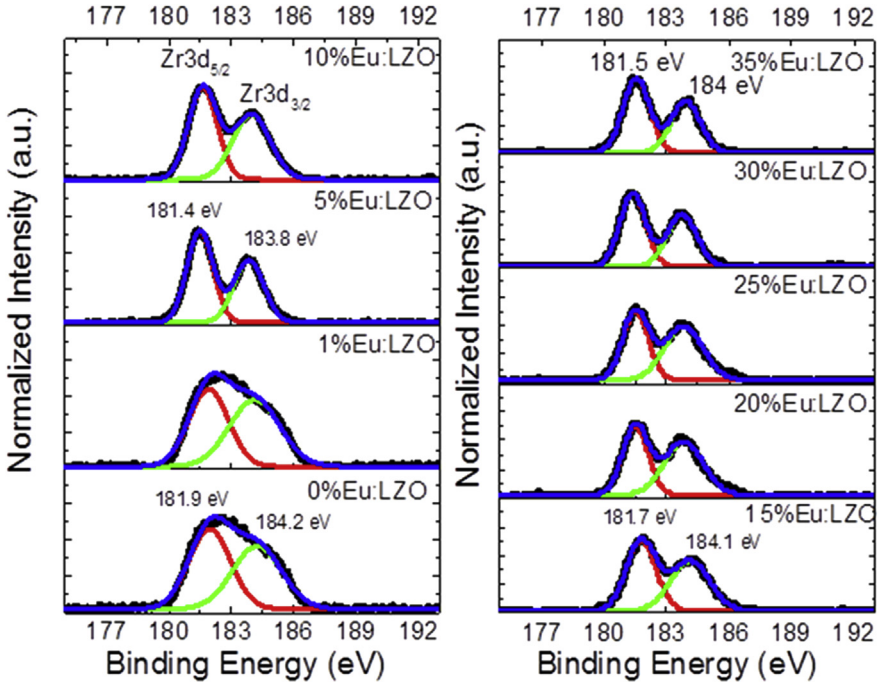


**Fig. 5.** Zr 3d XPS spectra of the as-prepared $La_2Zr_2O_7$:xmol%$Eu^{3+}$ NPs with x = 0, 1, 3, 5, 10, 15, 20, 25, 30 and 35.

consisted of two main peaks of 2d5/2 and 2d3/2 levels at 181.9 and 184.2 eV, respectively, resulting in a spin–orbit coupling (Δ) of 2.4 eV, which is comparable to that observed in related systems [48,59]. The undoped and 1% $Eu^{3+}$ doped $La_2Zr_2O_7$:x%$Eu^{3+}$ NPs showed broad XPS features of Zr 3d. This could be due to the non-uniform distribution of the $Zr^{4+}$ in the undoped and low $Eu^{3+}$ containing compositions in all available sites [56]. More distinct and narrowed Zr 3d peak with larger x in the $La_2Zr_2O_7$:x%$Eu^{3+}$ NPs indicated the more ordered nature of the zirconium chemical state in the $La_2Zr_2O_7$ NPs at higher $Eu^{3+}$ doping. Comparing with defect fluorite structure [23], it is truly ordered as expected from pyrochlore structure. To sum, these XPS results (Figs. 3–5) are consistent with the Raman data (Fig. 2).

The XPS spectra of $Eu^{3+}$ 3d (Fig. 6) were broad and could be due to either the exchange interaction between the 3d holes and partially filled 4f shell of $La^{3+}$ ion or the oxidized nature of $Eu^{3+}$ ions on the surface of the $La_2Zr_2O_7$:xmol%Eu NPs [60,61]. Here, no $Eu^{3+}$ 3d peak was detected for the $La_2Zr_2O_7$:xmol%Eu NPs with x = 1 and 5. This phenomenon was probably seen because XPS is surface sensitive technique and the measured signal is exponentially surface-weighted. Even the amount of $Eu^{3+}$ ions on the surface of the $La_2Zr_2O_7$:xmol%Eu NPs with x = 1 and 5 was undetectable by XPS, $Eu^{3+}$ was certainly present based on the EDX spectra (Fig. S3) and PL spectra (Figs. 8 and 9 shown below) of the corresponding $La_2Zr_2O_7$:1mol%Eu and $La_2Zr_2O_7$:5mol%Eu NPs. At higher $Eu^{3+}$ doping levels, the characteristic peak of $Eu^{3+}$ $3d_{5/2}$ (~1134.6 eV) was detected from the as-synthesized compositions ($La_2Zr_2O_7$:x%$Eu^{3+}$ with x = 10 to 35). This value was consistent with that reported on the literature, indicating that the oxidation states of europium ions of all the $La_2Zr_2O_7$:x%$Eu^{3+}$ NPs were +3 [62,63]. It also indicated more uniform nature of the europium dopant, which could be further related to the increase in surface area of $La_2Zr_2O_7$ NPs with the decrease in particle size induced by increased doping concentration of $Eu^{3+}$ (Table S5). No extra Eu phase has been detected on the surface of the $La_2Zr_2O_7$:xmol%Eu NPs through XPS analysis even for the highest $Eu^{3+}$ doped sample. This further ensured the doping of $Eu^{3+}$ ions at the La sites, irrespective of doping concentration in this particular $La_2Zr_2O_7$ host, and invalidated the assumption that $Eu^{3+}$ ion agglomeration at the surface of the NPs at higher doping $Eu^{3+}$ ions.

In addition, survey XPS spectra (ESI-6 and Fig. 7) were used to estimate the relative atomic percentage on the surface of the $La_2Zr_2O_7$:xmol%Eu NPs based on the areas under the La 3d, Zr 3d and Eu 3d peaks with the atomic sensitivity factors (ASF) provided by the XPS company (Thermo Scientific). It can be concluded that the ratio of the La: Zr: Eu is in close agreement with the initial precursors added for most of the compositions studied except 1 and 5 mol%Eu doped compositions. For example, the calculated ratio of La: Zr: Eu = 0.71: 1.0: 0.28 was in close agreement with the initial ratio of added precursors for the synthesis of the $La_2Zr_2O_7$:35%$Eu^{3+}$ NPs (La: Zr: Eu = 0.65: 1.0: 0.35). Although no $Eu^{3+}$ 3d peak was detected by XPS from the $La_2Zr_2O_7$:xmol%Eu NPs where x = 1 and 5, it can be anticipated the existence of $Eu^{3+}$ ions in these two compositions like in other samples as proved with the photoluminescence study discussed in later sections.

### 3.4. Photoluminescence properties of the $La_2Zr_2O_7$:xmol%$Eu^{3+}$ NP powders

Excitation spectra of the as-prepared $La_2Zr_2O_7$:xmol%$Eu^{3+}$ NPs with x = 1, 3, 5, 10, 15, 20, 25, 30 and 35 were collected by monitoring the $Eu^{3+}$ emission at 612 nm corresponding to $^7F_2 \rightarrow {}^5D_0$ transition (Fig. 8a). These excitation spectra all present a wide excitation band from 230 to 300 nm that corresponds to the charge transfer band (CT) transition and is attributed to $O^{2-}(2p) \rightarrow Eu^{3+}(4f)$ ligand-to-metal charge transfer. The 322 nm, 390 nm and 470 nm excitation bands correspond to the $Eu^{3+}$ (f–f) transitions. The relative intensity of the $O^{2-} \rightarrow Eu^{3+}$ CTB peak (~258 nm) was found to increase with increasing $Eu^{3+}$ doping concentration up to 5mol% $Eu^{3+}$ (Fig. 8b). For doping concentration higher than 5mol% $Eu^{3+}$, the peak intensity was found to decreasing slowly up to 15mol% Eu (Fig. 8b). However, a sharper decrease in excitation intensity corresponding to CTB was observed for the samples with doping levels higher than 20mol% $Eu^{3+}$. This may be due to an increase in

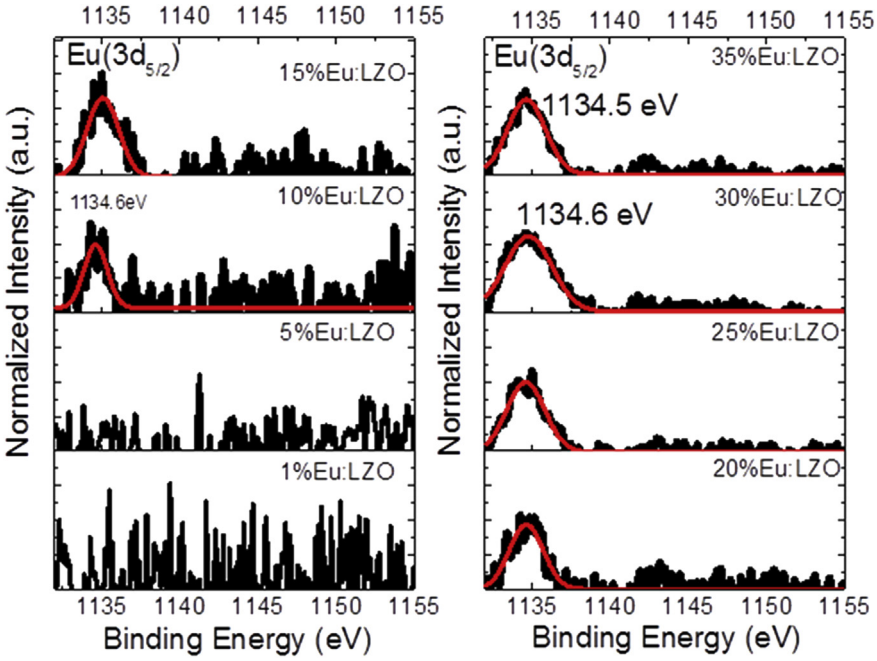


**Fig. 6.** Eu 3d XPS spectra of the as-prepared $La_2Zr_2O_7$:xmol%$Eu^{3+}$ NPs with x = 0, 1, 3, 5, 10, 15, 20, 25, 30 and 35.

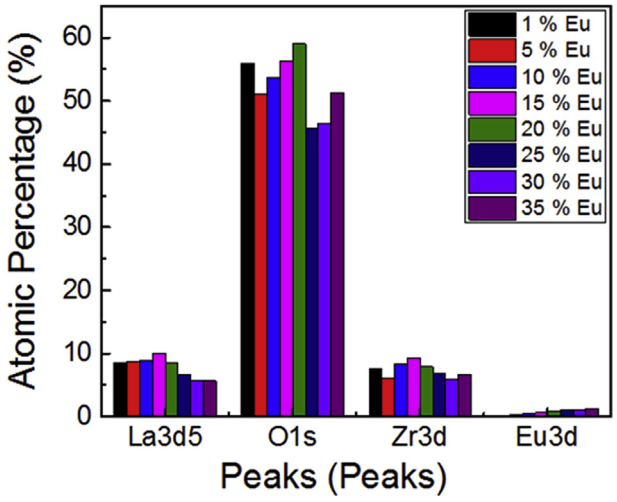


**Fig. 7.** The atomic percentage based on the XPS spectra of La 3d, O 1s, Zr 3d, and Eu 3d peaks from the as-prepared $La_2Zr_2O_7$:xmol%$Eu^{3+}$ NPs with x = 1, 3, 5, 10, 15, 20, 25, 30 and 35.

nonradiative ion-ion energy transfer and increased localized disorder at higher doping levels, which may cause energy migration and emission quenching [45].

Additionally, the charge transfer peak was red shifted at higher $Eu^{3+}$ concentrations and the maximum shift was found to be 6 nm for $La_2Zr_2O_7$:35%$Eu^{3+}$ as shown in Fig. 8a. It was obvious to observe such a shift in the CTB peak based on the metal to ligand environmental changes that occur with the change in the Eu:La ratio among the $La_2Zr_2O_7$:x%$Eu^{3+}$ NP samples [64]. Here, we propose that the red shift in the CTB is partially governed by the decrease in the lattice parameter due to the change in cation size as $Eu^{3+}$ replaces $La^{3+}$, especially for higher $Eu^{3+}$ doped samples compared to that of low doped samples (Fig. 8b). In addition, broadening could have minor effect on CTB shifting as observed in the similar study [65]. Importantly, the broadening pattern of the CTB band from the $La_2Zr_2O_7$:x%$Eu^{3+}$ NPs (Fig. 8b) was also consistent with the fact that there was a decrease of particle size as the doping concentration increased (Fig. S4 and Table S5).

Fig. 9 shows the emission spectra of $La_2Zr_2O_7$:xmol%$Eu^{3+}$ nanoparticles when excited with 258 nm corresponding to the charge-transfer band and the $Eu^{3+}$ (f–f) transition bands at 322 nm, 394 nm, and 465 nm. As can be seen in Fig. 9 and Fig. S10, the spectra consist of various sharp emission lines due to the direct excitation of the $Eu^{3+}$ ions from the ground level to higher levels of the 4f-manifold. All the as-prepared $La_2Zr_2O_7$:xmol%$Eu^{3+}$ NP samples showed the characteristic $Eu^{3+}$ emissions from the $^5D_2 \rightarrow {}^7F_3$, $^5D_1 \rightarrow {}^7F_i$ (where *i* runs from 0, to 2), and $^5D_0 \rightarrow {}^7F_j$ (where *j* runs from 0 to 4) transitions. The signals at 512, 527, 534, 552, 579–592, 612, 656, and 711 nm correspond to the $^5D_2 \rightarrow {}^7F_3$, $^5D_1 \rightarrow {}^7F_0$, $^5D_1 \rightarrow {}^7F_1$, $^5D_1 \rightarrow {}^7F_2$, $^5D_0 \rightarrow {}^7F_1$, $^5D_0 \rightarrow {}^7F_1$, $^5D_0 \rightarrow {}^7F_2$, $^5D_0 \rightarrow {}^7F_3$ and $^5D_0 \rightarrow {}^7F_4$ transitions of $Eu^{3+}$, respectively (See details ESI-7a). The $^5D_0 \rightarrow {}^7F_1$ and $^5D_0 \rightarrow {}^7F_3$ states are magnetic dipole transitions independent of the surrounding ions. The strongest emission corresponds to the hypersensitive electric dipole transition from $^5D_0 \rightarrow {}^7F_2$. Comparing to our previous studies, the site symmetry of $Eu^{3+}$ in $La_2Zr_2O_7$ has been identified as $D_{2d}$ with two $Eu^{3+}$ crystallographic sites [32]. The first site could be due to $Eu^{3+}$ ion replacing $Zr^{4+}$ antisites and second site could be due to the $Eu^{3+}$ ions replacing the regular $RE^{3+}$ sites. In general, $Eu^{3+}$ ions occupy at regular $La^{3+}$ sites due to matching ionic radius and oxidation state. However, there have been studies suggesting the high volume of cation antisite defects are due to difference in ionic radius ratio, lattice parameters, and the oxygen positional parameters in two metal cations based oxides such as $La_2Zr_2O_7$ [16,66]. In an ideal situation, we anticipate that initially $Eu^{3+}$ ions replace the $Zr^{4+}$ antisites, and upon reaching a threshold concentration most, if not all, of the antisites are filled. Above this critical concentration, impurities can replace regular La sites.

By comparing the PL spectra of the $La_2Zr_2O_7$:x%$Eu^{3+}$ samples, one could reveal how sensitive the $Eu^{3+}$ PL spectra were to the doping concentration. In addition, emission peak intensity was strongly dependent on dopant concentration as observed in Fig. 9.

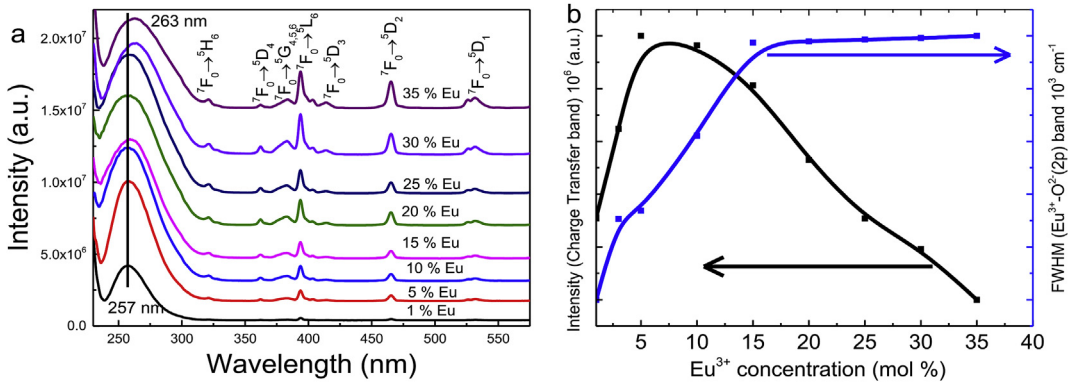


**Fig. 8.** (a) Excitation spectra of the as-prepared $La_2Zr_2O_7$:xmol%$Eu^{3+}$ NPs with x = 1, 3, 5, 10, 15, 20, 25, 30 and 35 by monitoring the $^5D_0 \rightarrow {}^7F_2$ (612 nm) emission. (b) Relative excitation intensity and FWHM variation of the $O^{2-} \rightarrow Eu^{3+}$ CTB peak (~258 nm) at different $Eu^{3+}$ concentrations.

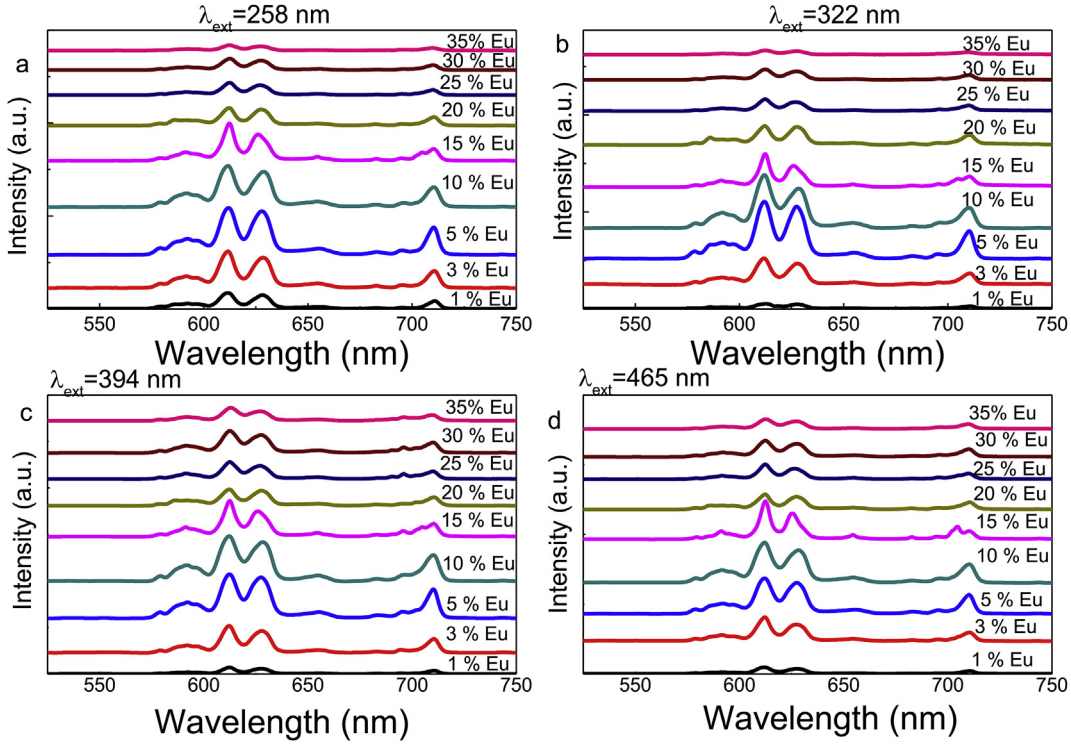


**Fig. 9.** Emission spectra of the as-prepared $La_2Zr_2O_7$:xmol%$Eu^{3+}$ NPs with x = 1, 3, 5, 10, 15, 20, 25, 30 and 35 at four different excitation wavelengths: 258 nm, 322 nm, 394 nm, and 465 nm.

For example, the intensity of the emission peak at 612 nm was found to decrease in the following excitation wavelength order: 258 nm > 394 nm > 465 nm > 322 nm (ESI-7b). From these results, it could be inferred that the energy transfer extents from the host to $Eu^{3+}$ ions and $Eu^{3+}$ ions to $Eu^{3+}$ ions depended on the concentration of $Eu^{3+}$ and the excitation wavelengths.

In conclusion, the large ionic size mismatch between $Zr^{4+}$ and $Eu^{3+}$ leads to distortion of the original lattice and breaks the inversion symmetry. The strongest emission corresponds to the hypersensitive electric dipole transition from $^5D_0 \rightarrow {}^7F_2$. The observed PL intensity differences between the samples clearly indicated that $Eu^{3+}$ doping concentration and excitation wavelengths plays an important role in getting highest photoluminescence emission from $La_2Zr_2O_7$:xmol%$Eu^{3+}$ NPs. At higher doping, the $La_2Zr_2O_7$:x%$Eu^{3+}$ samples exhibited weaker emissions compared to that of lower $Eu^{3+}$ doped counterparts. In addition, the intensity of the $^5D_0 \rightarrow {}^7F_2$ electric dipole transition was found to be stronger compared to that of $^5D_0 \rightarrow {}^7F_1$ magnetic dipole transition for all samples at all the excitations as shown in Fig. 9.

To quantify the dopant concentration effect, we also measured the absolute photoluminescence quantum yield (PLQY) as a function of the $Eu^{3+}$ doping percentage under 258 nm excitation (Table 1). It was observed that PLQY increased as $Eu^{3+}$ concentration increased from 1mol% to 5mol%. For higher $Eu^{3+}$ concentrations up to 35mol%, there was a decrease in PLQY. The decrease in the PLQY and associated decrease in PL intensity (ESI-7b) with the increase in $Eu^{3+}$ concentration could be attributed to the increased number of defects and concentration quenching mechanism. In the present study, quenching was dominating at or above 15%$Eu^{3+}$ doped NPs (ESI-7b), which was higher than the experimental value

**Table 1**
PLQY of the $La_2Zr_2O_7$:xmol%$Eu^{3+}$ NPs (x = 1, 3, 5, 10, 15, 20, 25, 30 and 35) at room temperature under 258 nm excitation after integrating the emission wavelength range from 500 to 750 nm.

| Samples | Average PLQY (%) |
|---|---|
| 1% Eu | 3.44 ± 0.34 |
| 3% Eu | 6.71 ± 0.67 |
| 5% Eu | 9.89 ± 0.98 |
| 10%Eu | 9.42 ± 0.94 |
| 15%Eu | 7.84 ± 0.78 |
| 20%Eu | 5.09 ± 0.70 |
| 25%Eu | 3.35 ± 0.33 |
| 30%Eu | 2.08 ± 0.20 |
| 35%Eu | 0.88 ± 0.088 |

obtained for $Eu^{3+}$:$Gd_2O_3$ [45]. This quenching effect can most likely be explained by an optimal distance of $Eu^{3+}$-$Eu^{3+}$ being reached at 5mol%, and higher concentrations leading to nonradiative energy dissipations [20]. Additionally, it is known that an increased dopant concentration can introduce defect states in nanoparticle hosts leading to defect based quenching, which may play a role in our samples as well [20].

### 3.5. Decay analysis

To quantify the effect of dopant $Eu^{3+}$ concentration on the luminescent dynamics of the $La_2Zr_2O_7$:x%$Eu^{3+}$ NPs, we calculated the effective lifetime ($\tau_{eff}$) by fitting the experimental decay curves (Fig. 10a) with a multi exponential function (ESI-8 and Table S9). Effective lifetime $\tau_{eff}$ as a function of the dopant concentration shown in Fig. 10b consisted of two concentration dependent patterns: (a) lifetime increases up to doping level of 10%$Eu^{3+}$ in the $La_2Zr_2O_7$:x%$Eu^{3+}$ NPs and (b) lifetime decreases rapidly above doping level of 15%$Eu^{3+}$ in the $La_2Zr_2O_7$:x%$Eu^{3+}$ NPs. These decay patterns clearly indicate that energy transfer and decay processes depended on the dopant concentration [40]. Furthermore, the fit of the kinetics for the $La_2Zr_2O_7$:x%$Eu^{3+}$ NPs at 612 nm showed average 28% contribution from the short ($\tau_1$) and 72% contribution from the long ($\tau_2$) component (Table S9) for samples with doping level lower than 15mol% of $Eu^{3+}$. At higher doping, lifetime contribution was reversed (Table S9). Based on the concept of phonon contribution, long component of the decay arises from $Eu^{3+}$ ions occupying 8-fold coordinated $La^{3+}$ site whereas short component can be ascribed to $Eu^{3+}$ ions occupying at $Zr^{4+}$ antisites. Lower photoluminescence QY with the increased contribution from short component of lifetime at higher $Eu^{3+}$ doping justifies our discussion on order-disorder (anion-disorder) transition at higher $Eu^{3+}$ doping in $La_2Zr_2O_7$. In addition, it justifies our previous assumption that initially $Eu^{3+}$ ion replaces the $Zr^{4+}$ antisites. The possible excitation and decay mechanisms are further supported by the proposed energy level diagram (Fig. S10).

In conclusion, PL spectra and decay analysis of the $La_2Zr_2O_7$:x% $Eu^{3+}$ samples indicated the presence of two $Eu^{3+}$ crystallographic sites. Increased contribution from short component of lifetime at higher $Eu^{3+}$ doping as shown in Table S9 clearly indicates the increase number of defects with higher $Eu^{3+}$ doping; the proposed concept is consistent with Raman analysis and PL analysis.

### 3.6. Emission properties under X-ray excitation

X-ray excited luminescence (XEL, Fig. 11a) was monitored for the selected $La_2Zr_2O_7$:x%$Eu^{3+}$ (x = 0, 1, 3, 5, 10, 15, 20, and 25) NP samples. In the X-ray excitation mode, it was the $La_2Zr_2O_7$ host that was excited, with the subsequent formation of a great number of electron-hole pairs that migrate within its structure [67]. The migration stage is strongly affected by defects, surfaces and interfaces that can introduce energy levels into the band gap of the host material [67]. The scintillation luminescence occurs when these electron-hole pairs recombine at the activator $Eu^{3+}$ sites with the net scintillation intensity being determined by the competition between radiative recombination at the Eu sites versus nonradiative recombination at quenching centers and trapping of the carriers. It was apparent from the evaluation of the optically and X-ray excited spectra that the XEL originated from the same $Eu^{3+}$ levels as in the optically excited PL emission. The XEL intensity varied with the $Eu^{3+}$ concentration (ESI-11) and the maximum luminescence intensity was observed for the $La_2Zr_2O_7$:5mol%$Eu^{3+}$ NPs, similar to the trend of the 612 emissions under 258 nm excitation (Fig. 9a).

Furthermore, ionizing radiation stability of the brightest XEL composition, i.e. $La_2Zr_2O_7$:5mol%$Eu^{3+}$ NPs, was tested under X-ray irradiation with a dose at the rate of 2.28 Gy/min for 1 h. Significant XEL intensity change (~45%) over time (1 h) indicated that $La_2Zr_2O_7$ is not a stable host under the X-ray radiation exposure (Fig. 11b). This is contrary to the stability observed for the same $La_2Zr_2O_7$:5mol%$Eu^{3+}$ NPs under UV exposure (inset of Fig. 11b). We anticipated that these ordered zirconate pyrochlore compositions become disordered (amorphous) due to disordering of the A and M site cations, i.e. by losing the long range order [68,69]. Similar amorphization behavior was observed for other pyrochlore compounds [70,71]. Although this preliminary study provided a basis for predicting the durability of zirconate pyrochlore as a

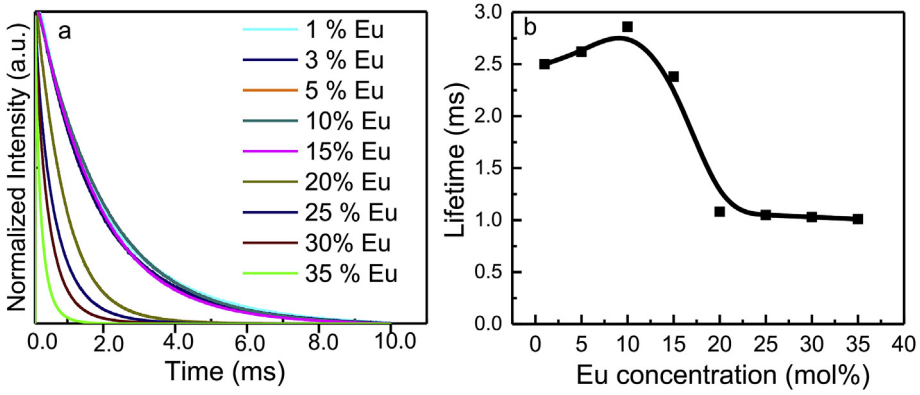


**Fig. 10.** (a) Fluorescent decay curves at $\lambda_{ex}$ = 258 nm and $\lambda_{em}$ = 612 nm, and (b) average lifetime as a function of dopant concentration of the $La_2Zr_2O_7$:xmol%$Eu^{3+}$ NPs with x = 1, 3, 5, 10, 15, 20, 25, 30 and 35.

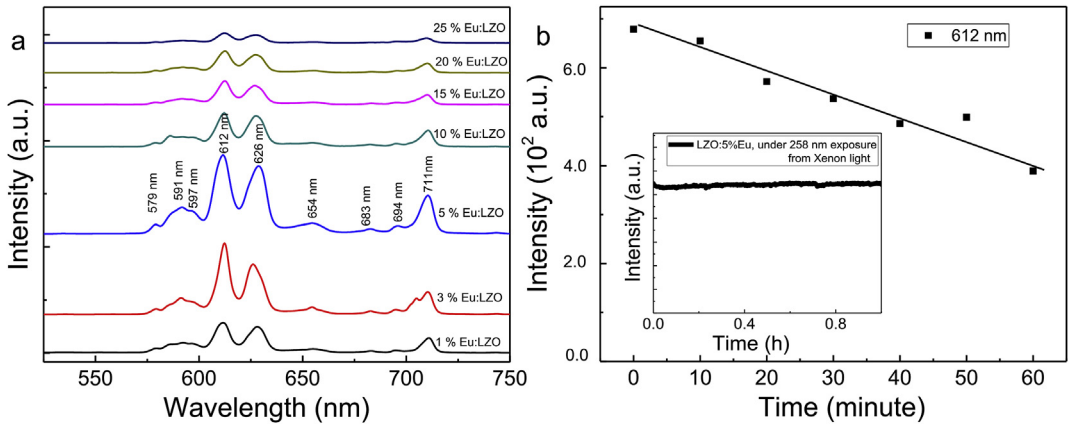


**Fig. 11.** (a) X-ray induced luminescence of the $La_2Zr_2O_7$:xmol%$Eu^{3+}$ NPs with x = 1, 3, 5, 10, 15, 20, and 25 excited with an X-ray source at ~130 kVp and 5 mA. (b) Variations of XEL intensity over exposure time for the red emission at 612 nm from the $La_2Zr_2O_7$:5mol%$Eu^{3+}$ NPs at an X-ray tube voltage of 130 KV and current of 5 mA. Inset shows the kinetic scan for the same $La_2Zr_2O_7$:5mol%$Eu^{3+}$ NPs under 258 nm excitation from a Xenon lamp.

scintillation host, it requires additional detailed experiments to explain these effects in the future.

## 4. Conclusions

In this paper, X-ray diffraction and Raman spectroscopy were used as complementary techniques for the study of the disordered fluorite and ordered pyrochlore structure of $La_2Zr_2O_7$:xmol%Eu NPs to provide information on short-range and long-range ordering, respectively. Raman analysis showed that the pyrochlore structure was favored for the $La_2Zr_2O_7$:xmol%Eu NPs at low $Eu^{3+}$ doping levels. Furthermore, Raman analysis demonstrated a gradual increase in localized anion disorder across the entire $La_2Zr_2O_7$ structure with higher $Eu^{3+}$ doping levels. We also reported the doping concentration dependence of the optical properties of the $La_2Zr_2O_7$:x%Eu NPs under both optical and X-ray excitations. The measured PL, PLQY, and fluorescence lifetimes of these $Eu^{3+}$ doped $La_2Zr_2O_7$ NPs with different doping levels demonstrated that there was fluorescence quenching for more than 5% $Eu^{3+}$ doping. Although the energy transfer process and amorphization under X-ray excitation have not been fully understood yet, our observation showed that these unique $La_2Zr_2O_7$:x%$Eu^{3+}$ NP systems deserve further investigation. These NPs also deserve a synthetic optimization in order to further understand the photoluminescence and scintillation relationship. To sum, the $Eu^{3+}$ related luminescence induced by multiple optical excitation combined with $La_2Zr_2O_7$ host properties, such as strong X-ray absorption, indicated that these high density $La_2Zr_2O_7$:xmol%$Eu^{3+}$ NPs are promising nanomaterials for various applications.

## Acknowledgments

The authors thank the support from the Defense Threat Reduction Agency (DTRA) of the U.S. Department of Defense (award #HDTRA1-10-1-0114) and the National Science Foundation under DMR grant #1523577 (PREM: UTRGV-UMN Partnership for Fostering Innovation by Bridging Excellence in Research and Student Success). The authors acknowledge the startup support from the STARs Program at the University of Texas System (M. Alcoutlabi).

## Appendix A. Supplementary data

Supplementary data related to this article can be found at http://dx.doi.org/10.1016/j.jallcom.2016.09.218.

## References

[1] D.K. Chatterjee, M.K. Gnanasammandhan, Y. Zhang, Small upconverting fluorescent nanoparticles for biomedical applications, Small 6 (2010) 2781–2795.
[2] X. Chen, G. Liu, The standard and anomalous crystal-field spectra of $Eu^{3+}$, J. Solid State Chem. 178 (2005) 419–428.
[3] J. Dhanaraj, R. Jagannathan, T.R.N. Kutty, C.-H. Lu, Photoluminescence Characteristics of $Y_2O_3$:$Eu^{3+}$ nanophosphors prepared using sol–gel thermolysis, J. Phys. Chem. B 105 (2001) 11098–11105.
[4] J.B. Gruber, U. Vetter, T. Taniguchi, G.W. Burdick, H. Hofsäss, S. Chandra, D.K. Sardar, Spectroscopic analysis of Eu3+ in single-crystal hexagonal phase AlN, J. Appl. Phys. 110 (2011) 023104.
[5] G. Kumar, M. Pokhrel, A. Martinez, D. Sardar, Synthesis and upconversion spectroscopy of Yb,Er doped $M_2O_2S$ (M = La, Gd, Y) phosphors, Sci. Adv. Mater. 4 (2012) 623–630.
[6] M. Pokhrel, G.A. Kumar, C.G. Ma, M.G. Brik, B.W. Langloss, I.N. Stanton, M.J. Therien, D.K. Sardar, Y. Mao, Electronic and optical properties of Er-doped $Y_2O_2S$ phosphors, J. Mater. Chem. C 3 (2015) 11486–11496.
[7] Z.-G. Zang, W.-X. Yang, Theoretical and experimental investigation of all-optical switching based on cascaded LPFGs separated by an erbium-doped fiber, J. Appl. Phys. 109 (2011) 103106.
[8] A.J. Steckl, J.M. Zavada, Photonic applications of rare-earth-doped materials, MRS Bull. 24 (1999) 16–20.
[9] K.E. Sickafus, R.W. Grimes, J.A. Valdez, A. Cleave, M. Tang, M. Ishimaru, S.M. Corish, C.R. Stanek, B.P. Uberuaga, Radiation-induced amorphization resistance and radiation tolerance in structurally related oxides, Nat. Mater 6 (2007) 217–223.
[10] M. Tang, K.S. Holliday, C. Jiang, J.A. Valdez, B.P. Uberuaga, P.O. Dickerson, R.M. Dickerson, Y. Wang, K.R. Czerwinski, K.E. Sickafus, Order-to-disorder phase transformation in ion irradiated uranium-bearing delta-phase oxides $RE_6U_1O_{12}$ (RE = Y, Gd, Ho, Yb, and Lu), J. Solid State Chem. 183 (2010) 844–848.
[11] A. Navrotsky, Thermochemical insights into refractory ceramic materials based on oxides with large tetravalent cations, J. Mater. Chem. 15 (2005) 1883–1890.
[12] Y. Bai, L. Lu, J. Bao, Synthesis and characterization of lanthanum zirconate nanocrystals doped with iron ions by a salt-assistant combustion method, J. Inorg. Organomet. Polym. Mater. 21 (2011) 590–594.
[13] F. Brisse, O. Knop, Pyrochlores. III. X-Ray, neutron, infrared, and dielectric studies of $A_2Sn_2O_7$ stannates, Can. J. Chem. 46 (1968) 859–873.
[14] P.E.R. Blanchard, R. Clements, B.J. Kennedy, C.D. Ling, E. Reynolds, M. Avdeev, A.P.J. Stampfl, Z. Zhang, L.-Y. Jang, Does local disorder occur in the pyrochlore zirconates? Inorg. Chem. 51 (2012) 13237–13244.
[15] M.A. Subramanian, G. Aravamudan, G.V. Subba Rao, Oxide pyrochlores — A review, Prog. Solid State Chem. 15 (1983) 55–143.
[16] K.E. Sickafus, R.W. Grimes, J.A. Valdez, A. Cleave, M. Tang, M. Ishimaru, S.M. Corish, C.R. Stanek, B.P. Uberuaga, Radiation-induced amorphization resistance and radiation tolerance in structurally related oxides, Nat. Mater. 6 (2007) 217–223.
[17] P.E.R. Blanchard, S. Liu, B.J. Kennedy, C.D. Ling, M. Avdeev, J.B. Aitken, B.C.C. Cowie, A. Tadich, Investigating the local structure of lanthanoid hafnates $Ln_2Hf_2O_7$ via diffraction and spectroscopy, J. Phys. Chem. C 117 (2013) 2266–2273.
[18] A. Chartier, C. Meis, J.-P. Crocombette, L.R. Corrales, W.J. Weber, Atomistic

modeling of displacement cascades in $La_2Zr_2O_7$ pyrochlore, Phys. Rev. B 67 (2003) 174102.
[19] X. Cheng, Z. Qi, T. Li, G. Zhang, C. Li, H. Zhou, Y. Wang, M. Yin, Infrared phonon modes and dielectric properties of $La_2Zr_2O_7$: comparing thin film to bulk material, Phys. Status Solidi (b) 249 (2012) 854–857.
[20] A. Kumar, S. Babu, A.S. Karakoti, A. Schulte, S. Seal, Luminescence properties of europium-doped cerium oxide nanoparticles: role of vacancy and oxidation states, Langmuir 25 (2009) 10998–11007.
[21] B. Liu, J. Wang, Y. Zhou, T. Liao, F. Li, Theoretical elastic stiffness, structure stability and thermal conductivity of $La_2Zr_2O_7$ pyrochlore, Acta mater. 55 (2007) 2949–2957.
[22] B. Mandal, A. Tyagi, Preparation and high temperature-XRD studies on a pyrochlore series with the general composition $Gd_{2-x}Nd_xZr_2O_7$, J. Alloys Compd. 437 (2007) 260–263.
[23] S. Oswald, K. Knoth, B. Holzapfel, Xps depth profiling investigations on $La_2Zr_2O_7$ layers prepared by chemical solution deposition, Microchim. Acta 156 (2006) 121–124.
[24] A. Zhang, M. Lü, G. Zhou, S. Wang, Y. Zhou, Combustion synthesis and photoluminescence of $Eu^{3+}$,$Dy^{3+}$-doped $La_2Zr_2O_7$ nanocrystals, J. Phys. Chem. Solids 67 (2006) 2430–2434.
[25] H. Zhou, D. Yi, Z. Yu, L. Xiao, Preparation and thermophysical properties of $CeO_2$ doped $La_2Zr_2O_7$ ceramic for thermal barrier coatings, J. Alloys Compd. 438 (2007) 217–221.
[26] Y. Mao, X. Guo, J.Y. Huang, K.L. Wang, J.P. Chang, Luminescent nanocrystals with $A_2B_2O_7$ composition synthesized by a kinetically modified molten salt method, J. Phys. Chem. C 113 (2009) 1204–1208.
[27] D. Chen, R. Xu, Hydrothermal synthesis and characterization of $La_2M_2O_7$ (M = Ti, Zr) powders, Mater. Res. Bull. 33 (1998) 409–417.
[28] H. Chen, Y. Gao, Y. Liu, H. Luo, Coprecipitation synthesis and thermal conductivity of $La_2Zr_2O_7$, J. Alloys Compd. 480 (2009) 843–848.
[29] H. Xiao, X.T. Zu, F. Gao, W.J. Weber, First-principles study of energetic and electronic properties of $A_2Ti_2O_7$ (A = Sm, Gd, Er) pyrochlore, J. Appl. Phys. 104 (2008) 073503–073506.
[30] O. Rabin, J.M. Perez, J. Grimm, G. Wojtkiewicz, R. Weissleder, An X-ray computed tomography imaging agent based on long-circulating bismuth sulphide nanoparticles, Nat. Mater. 5 (2006) 118–122.
[31] J. Hainfeld, D. Slatkin, T. Focella, H. Smilowitz, Gold nanoparticles: a new X-ray contrast agent, Br. J. Radiol. 79 (939) (2006) 248–253.
[32] M. Pokhrel, M.G. Brik, Y. Mao, Particle Size, Crystal Phase, Dependent photoluminescence of $La_2Zr_2O_7$: $Eu^{3+}$ nanoparticles, J. Am. Ceram. Soc. 98 (2015) 3192–3201.
[33] C. Jiang, C. Stanek, K. Sickafus, B. Uberuaga, First-principles prediction of disordering tendencies in pyrochlore oxides, Phys. Rev. B 79 (2009) 104203.
[34] N. Li, H. Xiao, X.T. Zu, L.M. Wang, R.C. Ewing, J. Lian, F. Gao, First-principles study of electronic properties of $La_2Hf_2O_7$ and $Gd_2Hf_2O_7$, J. Appl. Phys. 102 (2007) 063704–063706.
[35] W.R. Panero, L. Stixrude, R.C. Ewing, First-principles calculation of defect-formation energies in the $Y_2$(Ti, Sn, Zr)$_2O_7$ pyrochlore, Phys. Rev. B 70 (2004) 054110.
[36] S.B. Alaparthi, L. Lu, Y. Tian, Y. Mao, Europium doped lanthanum zirconate nanoparticles with high concentration quenching, Mater. Res. Bull. 49 (2014) 114–118.
[37] N. Chang, J. Gruber, Spectra and energy levels of $Eu^{3+}$ in $Y_2O_3$, J. Chem. Phys. 41 (1964) 3227–3234.
[38] J.B. Gruber, R.P. Leavitt, C.A. Morrison, N.C. Chang, Optical spectra, energy levels, and crystal field analysis of tripositive rare earth ions in $Y_2O_3$. IV. $C_{3i}$ sites, J. Chem. Phys. 82 (1985) 5373–5378.
[39] Z. Lu, J. Wang, Y. Tang, Y. Li, Synthesis and photoluminescence of $Eu^{3+}$-doped $Y_2Sn_2O_7$ nanocrystals, J. Solid State Chem. 177 (2004) 3075–3079.
[40] O. Meza, E.G. Villabona-Leal, L.A. Diaz-Torres, H. Desirena, J.L. Rodríguez-López, E. Pérez, Luminescence concentration quenching mechanism in $Gd_2O_3$:$Eu^{3+}$, J. Phys. Chem. A 118 (2014) 1390–1396.
[41] H.J. Song, L.Q. Zhou, Y. Huang, L. Li, T. Wang, L. Yang, Synthesis, characterization and luminescent properties of $La_2Zr_2O_7$:$Eu^{3+}$ nanorods, Chin. J. Chem. Phys. 26 (2013) 83–87.
[42] Wei, Sun, Liao, Yin, Jiang, Yan, S. Lü, Size-dependent chromaticity in $YBO_3$:Eu nanocrystals: correlation with microstructure and site symmetry, J. Phys. Chem. B 106 (2002) 10610–10617.
[43] Y. Yang, Z. Li, Z. Li, F. Jiao, X. Su, D. Ge, White light emission, quantum cutting, and afterglow luminescence of $Eu^{3+}$-doped $Ba_5Gd_8Zn_4O_{21}$, J. Alloys Compd. 577 (2013) 170–173.
[44] M. Zhuravleva, B. Blalock, K. Yang, M. Koschan, C.L. Melcher, New single crystal scintillators: $CsCaCl_3$:Eu and $CsCaI_3$:Eu, J. Cryst. Growth 352 (2012) 115–119.
[45] E.M. Goldys, K. Drozdowicz-Tomsia, S. Jinjun, D. Dosev, I.M. Kennedy, S. Yatsunenko, M. Godlewski, Optical characterization of Eu-doped and undoped $Gd_2O_3$ nanoparticles synthesized by the hydrogen flame pyrolysis method, J. Am. Chem. Soc. 128 (2006) 14498–14505.
[46] R. Gunawidjaja, T. Myint, H. Eilers, Stabilization of tetragonal phase in $ZrO_2$:Eu by rapid thermal heating, Chem. Phys. Lett. 515 (2011) 122–126.
[47] S.K. Gupta, M.K. Bhide, S.V. Godbole, V. Natarajan, Probing site symmetry around $Eu^{3+}$ in nanocrystalline $ThO_2$ using time resolved emission spectroscopy, J. Am. Ceram. Soc. 97 (2014) 3694–3701.
[48] V. Narayanan, K. De Buysser, E. Bruneel, I.V. Driessche, X-ray photoelectron spectroscopy (XPS) depth profiling for evaluation of $La_2Zr_2O_7$ buffer layer capacity, Materials 5 (2012) 364–376.
[49] J. Chen, J. Lian, L. Wang, R. Ewing, R. Wang, W. Pan, X-ray photoelectron spectroscopy study of disordering in $Gd_2(Ti_{1-x}Zr_x)_2O_7$ pyrochlores, Phys. Rev. Lett. 88 (2002) 105901.
[50] S.B. Alaparthi, Y. Tian, Y. Mao, Synthesis and photoluminescence properties of $La_2Zr_2O_7$:$Eu^{3+}$@$YBO_3$ core@shell nanoparticles, Nanotechnology 25 (2014) 025703.
[51] M. Pokhrel, K. Wahid, Y. Mao, Systematic studies on $RE_2Hf_2O_7$:5%$Eu^{3+}$ (RE = Y, La, Pr, Gd, Er, and Lu) nanoparticles: effects of the A-site $RE^{3+}$ cation and calcination on structure and photoluminescence, J. Phys. Chem. C 120 (2016) 14828–14839.
[52] M. Glerup, O.F. Nielsen, F.W. Poulsen, The structural transformation from the pyrochlore structure, $A_2B_2O_7$, to the fluorite structure, $AO_2$, studied by raman spectroscopy and defect chemistry modeling, J. Solid State Chem. 160 (2001) 25–32.
[53] Y. Tong, S. Zhao, W. Feng, L. Ma, A study of Eu-doped $La_2Zr_2O_7$ nanocrystals prepared by salt-assistant combustion synthesis, J. Alloys Compd. 550 (2013) 268–272.
[54] Y. Tong, Y. Wang, Z. Yu, X. Wang, X. Yang, L. Lu, Preparation and characterization of pyrochlore $La_2Zr_2O_7$ nanocrystals by stearic acid method, Mater. Lett. 62 (2008) 889–891.
[55] B. Mandal, N. Garg, S.M. Sharma, A. Tyagi, Preparation, XRD and Raman spectroscopic studies on new compounds $RE_2Hf_2O_7$ (RE = Dy, Ho, Er, Tm, Lu, Y): pyrochlores or defect-fluorite? J. Solid State Chem. 179 (2006) 1990–1994.
[56] B.E. Scheetz, W.B. White, Characterization of anion disorder in zirconate $A_2B_2O_7$ compounds by Raman spectroscopy, J. Am. Ceram. Soc. 62 (1979) 468–470.
[57] K. Holliday, S. Finkeldei, S. Neumeier, C. Walther, D. Bosbach, T. Stumpf, TRLFS of $Eu^{3+}$ and $Cm^{3+}$ doped $La_2Zr_2O_7$: a comparison of defect fluorite to pyrochlore structures, J. Nucl. Mater. 433 (2013) 479–485.
[58] B.V. Kumar, R. Velchuri, G. Prasad, B. Sreedhar, K. Ravikumar, M. Vithal, Preparation, characterization, photoactivity and XPS studies of $Ln_2ZrTiO_7$ (Ln = Sm and Nd), Ceram. Int. 36 (2010) 1347–1355.
[59] B.V. Kumar, R. Velchuri, G. Prasad, B. Sreedhar, K. Ravikumar, M. Vithal, Preparation, characterization, photoactivity and XPS studies of $Ln_2ZrTiO_7$ (Ln = Sm and Nd), Ceram. Int. 36 (2010) 1347–1355.
[60] S. Fujihara, K. Tokumo, Multiband orange-red luminescence of $Eu^{3+}$ ions based on the pyrochlore-structured host crystal, Chem. Mater. 17 (2005) 5587–5593.
[61] J. Xu, X.H. Huang, N.L. Zhou, J.S. Zhang, J.C. Bao, T.H. Lu, C. Li, Synthesis, XPS and fluorescence properties of $Eu^{3+}$ complex with polydimethylsiloxane, Mater. Lett. 58 (2004) 1938–1942.
[62] H. Li, Y. Ding, Y. Wang, Photoluminescence properties of $Eu^{3+}$-exchanged zeolite L crystals annealed at 700 °C, CrystEngComm 14 (2012) 4767–4771.
[63] L. Lin, X. Sun, Y. Jiang, Y. He, Sol-hydrothermal synthesis and optical properties of $Eu^{3+}$, $Tb^{3+}$-codoped one-dimensional strontium germanate full color nano-phosphors, Nanoscale 5 (2013) 12518–12531.
[64] J.H. Lin, L.P. You, G.X. Lu, L.Q. Yang, M.Z. Su, Structural and luminescent properties of $Eu^{3+}$ doped $Gd_{17.33}(BO_3)_4(B_2O_5)_2O_{16}$, J. Mater. Chem. 8 (1998) 1051–1054.
[65] X. Liu, L. Li, H.M. Noh, B.K. Moon, B.C. Choi, J.H. Jeong, Chemical bond properties and charge transfer bands of $O^{2-}$-$Eu^{3+}$, $O^{2-}$-$Mo^{6+}$ and $O^{2-}$-$W^{6+}$ in $Eu^{3+}$-doped garnet hosts $Ln_3M_5O_{12}$ and $ABO_4$ molybdate and tungstate phosphors, Dalton Trans. 43 (2014) 8814–8825.
[66] L. Chen, X. Su, Y. Li, First-Principles study on cation-antisite defects of stannate and titanate pyrochlores, Open Access Libr. J. 1 (2014) 1–8.
[67] D. Avram, B. Cojocaru, M. Florea, V. Teodorescu, I. Tiseanu, C. Tiseanu, NIR to Vis-NIR up-conversion and X-ray excited emission of Er doped high Z BiOCl, Opt. Mater. Express 5 (2015) 951–962.
[68] G.R. Lumpkin, R.C. Ewing, Alpha-decay damage in minerals of the pyrochlore group, Phys. Chem. Minerals 16 (1988) 2–20.
[69] J. Lian, X. Zu, K.G. Kutty, J. Chen, L. Wang, R. Ewing, Ion-irradiation-induced amorphization of $La_2Zr_2O_7$ pyrochlore, Phys. Rev. B 66 (2002) 054108.
[70] B.P. Uberuaga, M. Tang, C. Jiang, J.A. Valdez, R. Smith, Y. Wang, K.E. Sickafus, Opposite correlations between cation disordering and amorphization resistance in spinels versus pyrochlores, Nat. Commun. 6 (2015) 8750.
[71] S. Yudintsev, S. Stefanovsky, B. Nikonov, M. Nikol'skii, T. Livshits, Potential matrices for immobilization of the rare earth-actinide fraction of high-level waste in the $RE_2Zr_2O_7$-$RE_2Ti_2O_7$ system, Radiochemistry 57 (2015) 187–199.